BNL-220560-2020-JAAM

Beam characterization at NSRL for radiobiological experiments - phase 1

L. Burigo, M. Sivertz

To be published in "Journal of Instrumentation"

October 2020

Collider Accelerator Department

Brookhaven National Laboratory

U.S. Department of Energy

USDOE Office of Science (SC), Nuclear Physics (NP) (SC-26)

DISCLAIMER

Beam characterization at NSRL for radiobiological experiments – phase 1

L. Burigo[a,b,1] **T. Gehrke**[a,b] **O. Jäkel**[a,b,c] **M. Sivertz**[d] **T. Olsen**[d] **A. Rusek**[d] **C. Obcemea**[e] **and S. Greilich**[a,b,2]

[a] *German Cancer Research Center (DKFZ), Heidelberg, Germany*

[b] *National Center for Radiation Research in Oncology (NCRO), Heidelberg Institute for Radiation Oncology (HIRO) Heidelberg, Germany*

[c] *Heidelberg Ion-Beam Therapy Centre (HIT) Heidelberg, Germany*

[d] *NASA Space Radiation Laboratory, Brookhaven National Laboratory, Upton, New York, USA*

[e] *Radiation Research Program, Division of Cancer Treatment and Diagnosis, National Cancer Institute, National Institutes of Health, Bethesda, Maryland, USA*

E-mail: L.Burigo@dkfz-heidelberg.de

Abstract: An experimental campaign was carried out at the NASA Space Radiation Laboratory to perform an additional, independent dosimetric characterization of the beams of protons, helium and carbon ions for radiobiological experiments. The campaign was undertaken by the request and with the support from the National Cancer Institute, US. In this initial phase, the goals were to obtain a first assessment of the dosimetric reproducibility of the beam control system, including analysis of spatial homogeneity and evaluation of ion beam contamination. They should facilitate the design of further experimental campaigns for beam characterization for radiobiological experiments. Measurements included reference dosimetry with comparison of in-house and external ionization chambers and electrometers, lateral-dose profile measurements in air, depth-dose profile in a water tank, evaluation of water equivalent thickness of a HDPE binary range shifter and estimation of impurities of the investigated helium-ion beam. The experiments and results are presented.

Keywords: Dosimetry concepts and apparatus, Detector alignment and calibration methods, Radiotherapy concepts, Instrumentation for heavy-ion therapy

[1] Corresponding author.

[2] Current address: Berthold Technologies GmbH & Co. KG, Calmbacher Straße 22, 75323 Bad Wildbad, Germany

Contents

1 Background

The increasing number of ion-beam therapy facilities worldwide[1] and their encouraging clinical results have led to a growing interest in research projects connected to ion-beam radiotherapy in the US. Consequently, the NASA Space Radiation Laboratory (NSRL)[1, 2] at Brookhaven National Laboratory — the only US research facility providing high-energy heavy-ion beams – is increasingly used for basic radiobiological research with heavy ions in the context of ion-beam therapy[3]. The results of these experiments may be used to generate a rationale for the clinical use of heavy-ion beams in the US. Therefore, it is of great importance to ensure the limitations of the generated data. Accurate knowledge of beam properties and dosimetry parameters is key for establishing the accuracy of these studies and to enable intercomparison and reproducibility[4, 5]. In this framework, the National Cancer Institute launched a program for an independent characterization of the ion beams delivered at NSRL and used for radiobiological experiments. As part of this initiative, a team of researchers from the German Cancer Research Center (DKFZ) conducted a series of measurements from February 28, 2019 to March 1, 2019 using equipment complementary to devices at NSRL. These first phase experiments focused on reference dosimetry, beam

[1] Current facilities in operation and patient statistics as reported by the Particle Therapy Co-Operative Group is available at https://www.ptcog.ch/

shape and potential contamination of the ion beams, as these are considered key factors for accurate dosimetry.

2 Material and Methods

2.1 Ion beams

NSRL provides ion beams from protons to gold nuclei, which are extracted from the Booster synchrotron of Brookhaven National Laboratory with energies from 50 to 1,500 MeV/n (up to 2,500 MeV for protons). For radiation therapy-related research, the species of interest are protons to neon ions with energies up to around 500 MeV/n available at dose rates up to around 4 Gy/min (depending on ion species and field size). The sources used to produce the ions are either a LINAC (for protons) or the Electron Beam Ion Source (EBIS) equipped with gas sources like helium and a laser ion source for any type of solid target, which can quickly change ion species within a few pulses. Beams produced from the laser ion source are especially susceptible to contamination from other ions with the same charge to mass ratio as the primary ion. Furthermore, traces of atmospheric gases like nitrogen, oxygen, and carbon are almost always present in the source vacuum chamber and are common contaminants. When accelerating helium it is also not unusual to find neon contamination in the gas cylinder supplying the helium gas to the source chamber.

The ion beams at NSRL are delivered by a horizontal beamline through a set of magnetic dipole, quadrupole and octupole lenses, which control the size and shape of the beam to match the desired radiation field. A large tungsten collimator may be used to control the overall field size and additional small collimators may be inserted, if a small pencil-beam is needed. The beam energy can be actively changed by modifying the synchrotron settings, or passively with the use of a binary range shifter placed in the beamline inside the experimental room. The binary range shifter is made of high-density polyethylene (HDPE). Additionally, modulator wheels may be inserted in the beamline to produce a spread-out Bragg peak (SOBP). In the set of experiments reported in this work, the field size was tuned to irradiate a 20×20 cm^2 area, whose fluence homogeneity was monitored with the digital beam imager (DBI). The DBI consists of a luminescence screen which is read out by an optical system and a CCD camera. The DBI is inserted in the beamline just behind the position where measurements are taken, and displays beam uniformity with a typical homogeneity of 3% throughout the inner part of the field.

In this first set of investigations, mainly mono-energetic beams were used. One of the available beam modulator wheels was also tested in the measurements. The following ion beams with approximately 20 cm range in water were used in the experiments: 173 MeV protons, 173 MeV/n helium ions, and 326 MeV/n carbon ions.

When a beam is requested, the number of ions to be delivered is specified and the irradiation is controlled by a first large area monitor chamber (usually QC3 chamber, see Table 1). The chamber reading is used as a reference signal to control the beam and provides a normalization (i.e dose and ions fluence delivered) for each irradiation that allows a direct comparison between different experiments. The monitor chamber is routinely calibrated

against a NIST calibrated ionization chamber prior to each run (usually "EGG600", see Table 1).

2.2 Equipment

The laboratory equipment used in the experiments is listed in Table 1. For the reference dosimetry experiments, Far West ionization chambers currently used at NSRL and two Farmer chambers were used in combination with 3 different readout electrometers. Lateral-dose profiles in air were measured with a small-sized cylindrical PinPoint chamber, while depth-dose profiles in water were obtained using a plane-parallel Markus chamber. In both profile measurements, the field chambers were fixed to a motorized arm in a phantom tank allowing accurate positioning of the chamber in the field. Last, a set of 3 Timepix silicon pixel detectors were mounted as a telescope device, providing an identification of the individual ion tracks for an evaluation of the beam contaminants. The detector technology named Timepix was developed at the European Organization for Nuclear Research (CERN) within the Medipix2 Collaboration[6, 7]. Its high granularity (pixel dimensions of 55 µm×55 µm) and a time resolution down to 10 ns facilitates single-particle detection. These features combined with the energy-sensitivity of each pixel have already enabled many applications with respect to ion detection, e.g. for radiation monitoring in space [8–10], for detection and tracking of secondary ions during ion-beam therapy [11–13], or as a part of detection systems developed for ion imaging[14].

All equipment from DKFZ (except the Timepix detector equipment) was calibrated and certified in December 2018 by PTW (Freiburg, Germany), to ensure correct functioning and traceability of the measured doses to the German national primary standard for dose, which is also the basis for ion-beam radiotherapy in Germany. The same type of equipment is used routinely at the Heidelberg Ion-Beam Therapy Center in daily clinical practice for ion-beam dosimetry.

2.3 Reference dosimetry

Reference dosimetry measurements were performed to compare the response of the ionization chambers used at NSRL, Far West Technology "EGG" (S/N 600 and S/N 908), against the calibrated ionization chambers PTW 30013 Farmer. To account for possible impact of the readout, different devices were used, namely the 2 recycling integrators from NSRL ("EGG1" and "EGG2") and the PTW UNIDOS Electrometer T10021. In all the experiments, the chamber "EGG" (S/N 600) and the recycling integrator "EGG1" were used as reference. Measurements were performed for 173 MeV proton and 326 MeV/n carbon-ion beams. The chambers were mounted with build-up cap and placed at the same distance from the beam window which correspond to the position typically used for the radiobiological experiments (see Figure 1). A second set-up made use of the PTW 30013 Farmer chambers placed in a RW3 slab phantom with the "EGG" chambers located directly upstream of the phantom. The readout from the UNIDOS$^{\text{webline}}$ electrometer was accessed remotely using the corresponding VNC viewer. In total, 298 measurements from 145 irradiations in 16 runs were performed, accounting for 13 out of the 24 possible permutations of chamber/readout/beam (see Figure 2). Multiple measurements of each permutation were not feasible due to time

Table 1. Laboratory equipment from NSRL and complementary equipment from DKFZ used in the experiments.

Equipment	Comments
Equipment from NSRL	
Far West Technology "EGG" Ionization Chamber	S/N: 600, NIST calibrated ionization chamber, 1 cm^3 nominal sensitive volume, used as reference chamber in the experiments for relative comparisons, in the following denominated as "EGG600"
Far West Technology "EGG" Ionization Chamber	S/N: 908, 1 cm^3 nominal sensitive volume, in the following denominated as "EGG908"
"EGG1" Recycling Integrator	Used as reference electrometer in the experiments for relative comparisons
"EGG2" Recycling Integrator	
Monitor chamber QC1	Large planar ion chamber located approximately 10 cm from vacuum window. Used in combination with QC3 and binary range shifter to measure Bragg curves
Monitor chamber QC3	QC3 chamber used to cut-off the irradiation located approximately 500 cm from vacuum window
Binary Range Shifter	Set of remotely-driven HDPE layers with thickness varying from 0.25 mm to 128 mm
Luminescence Screen	Scintillator camera
Beam Modulator Wheel	Custom made for modulation of 1.2 cm SOBP for carbon-ion beam
Collimators	Blocks of tungsten
Equipment from DKFZ	
2 PTW Farmer-type Ionization Chambers	S/N: TM30013-03641 and TM30013-001583, 0.6 cm^3 nominal sensitive volume
2 PTW Markus-type Ionization Chambers	S/N: TM34045-0318 and TM34045-0615, 0.02 cm^3 nominal sensitive volume
1 PTW Pinpoint Ionization Chamber	S/N: TM31014-0015, 0.015 cm^3 nominal sensitive volume
PTW TANDEM Electrometer	S/N: T10011-10365
PTW UNIDOS^{webline} Electrometer	S/N: T10021-0269
PTW MP3 phantom tank	Remote-controlled 3D acrylic water tank with 20 mm thick walls and a scanning range of 60×50×40.8 cm^3.
PTW TBA Control Unit	S/N: T41013-0623
PTW TRUFIX base set	S/N: 981150
PTW RW3 slab phantom	Farmer chamber slab 29672/U19
PTW MEPHYSTO mc2 software	Version 1.8.0
3 Timepix detectors	Silicon pixel detectors with 55 µm pixel pitch, 300 µm sensor thickness, first generation; S/N: SPN3-3G1 (E07-W167), SPN3-3F6 (C07-W167), SPN3-3E4 (C08-W167)
1 FITPIX read-out interface	For read-out of Timepix detectors. S/N: FITPIX 0022
Pixet software	For data acquisition and steering of Timepix detectors. Version 1.4.7

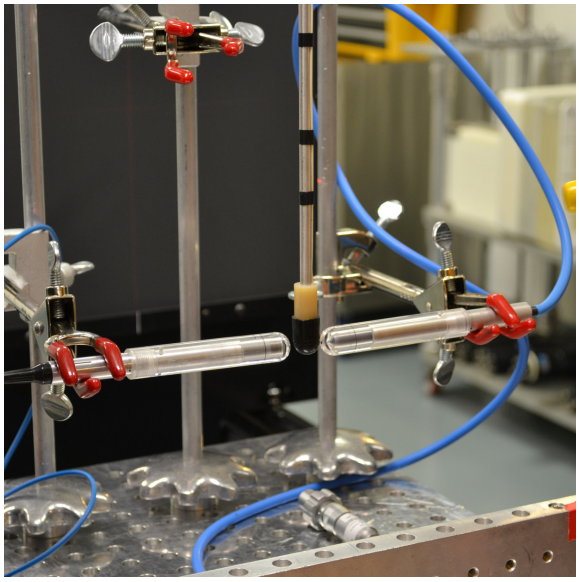

Figure 1. Set-up with the vertically-positioned reference chamber "EGG600" and two horizontally-positioned Farmer chambers.

limitations. The primary focus of the experiment was the comparison of the main ionization chamber and electrometers from NSRL and PTW for carbon ions. As a secondary goal, differences between carbon ions and protons as well as between the main and the second ionization chamber from NSRL were investigated. Measurements were performed for requested doses of 0.1 Gy (carbon-ion beam) and 0.2 Gy (proton beam). These values are well within the linear range of the ionization chambers and allow low uncertainty with shorter delivery time compared to the higher doses used in radiotherapy and radiobiological experiments.

2.4 Dose profiles

Dose profiles were performed using a MP3 phantom tank mounted with a TBA control unit for remote positioning of the field chamber mounted inside the tank. A reference chamber was mounted upstream of the tank and positioned in such a way to not shadow the field chamber. The readout data were remotely collected using the tbaScan application from MEPHYSTO software. The electrometer was reset before the data collection in every run. Measurements were taken on time basis with the time being equal to an integer multiple of the cycle time of the accelerator. Dose profiles in a plane perpendicular to the beam axis, henceforth denominated lateral-dose profiles, were taken to evaluate the uniformity of the dose in the central part of the beam. Lateral-dose profiles in air were measured using a TM34045 Markus chamber (S/N 0318) as reference chamber and a TM31014 PinPoint chamber (S/N 0015) as field chamber. Depth-dose profile measurements were performed by filling the MP3 phantom tank with demineralized water and using 2 TM34045 Markus chambers (S/N 0318 used as reference chamber, S/N 0615 used as field chamber). Measurements were also performed for a SOBP using a modulator wheel in which case the

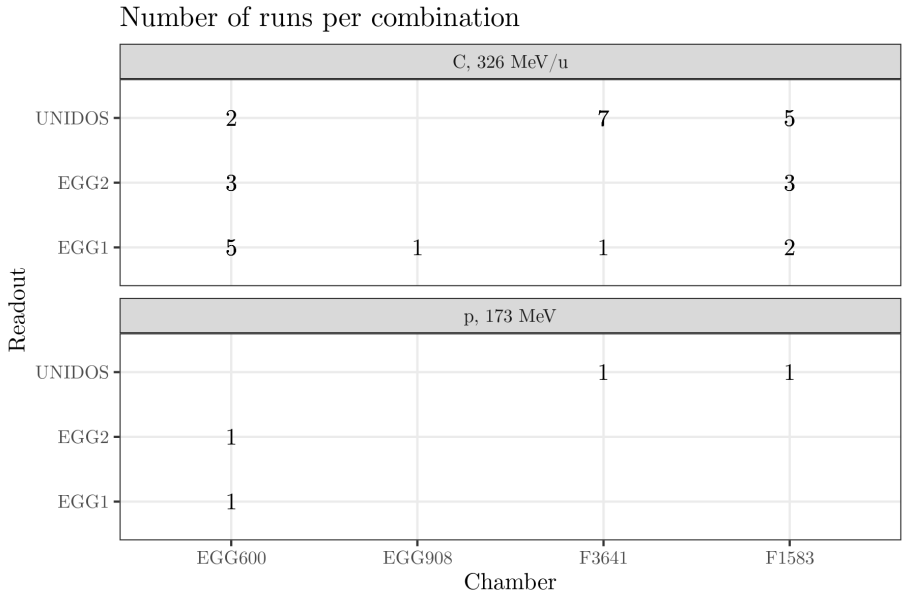

Figure 2. Number of runs per combination of chamber and readout device for carbon-ion beam (upper panel) and proton beam (lower panel).

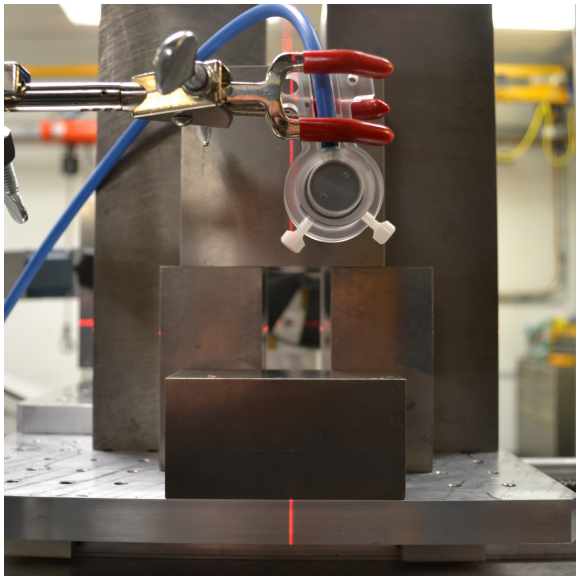

Figure 3. Set-up for measurements of SOBP. The reference TM34045 Markus chamber with build-up cap is displayed upstream of the collimator. The modulator wheel can be seen through the gap of the collimation.

beam was collimated downstream of the reference chamber. The beam modulator wheel and collimators were positioned in such a way that the modulated beam was aligned with the field chamber in the beam-eye-view (cf. Figure 3).

2.5 WET determination of binary range shifter layers

Since the binary range shifter mounted in the beamline is typically used at NSRL to passively change the energy of the ion beam or to measure depth-dose curves for range estimation, it is relevant to evaluate the water-equivalent thickness (WET) of the layers. The WET_i of each layer i was estimated by the changes of R_{80}[2] range in water as follows

$$\mathrm{WET}_i = \mathrm{R}_{80,\mathrm{ref}} - \mathrm{R}_{80,i}$$

where $\mathrm{R}_{80,\mathrm{ref}}$ corresponds to the range of a 326 MeV/n carbon ion beam in water, and $\mathrm{R}_{80,i}$ the range after traversing the layer i. The estimation of WET could also be used to evaluate the water-equivalent path length (WEPL) in HDPE as follows

$$\mathrm{WEPL} = \frac{(\mathrm{R}_{80,\mathrm{ref}} - \mathrm{R}_{80})}{\text{layer thickness}}.$$

2.6 Beam impurity

Analysis of contamination for a 173 MeV/n helium-ion beam was performed using a set of Timepix silicon pixel detectors in order to obtain an initial estimation of the purity of the beam. This study is not representative of all beam species at NSRL. However, traces of atmospheric gases in the helium-ion beam indicate possible contaminants in ion beams with the same charge-mass ratio (e.g. carbon-ion beam). The aim was to determine if other ion types heavier than helium ions are present in the requested helium-ion beam, and if so, the relative amount of the contaminants. The presence and quantity of lighter fragments produced inevitably by nuclear fragmentation in beamline elements and air downstream of the synchrotron was not investigated. General aspects of nuclear fragmentation in the context of ion-beam therapy can be found in [15], and current research specific to helium-ion fragmentation in [16–18].

The energy deposition of individual ion tracks in the 300-µm-thick silicon layer of the Timepix detectors was measured to differentiate between ion types. In general, the mean energy deposition of mono-energetic ion beams in matter is well described by the Bethe-Bloch equation[19, 20], which is given below without the shell or density correction terms:

$$\left\langle \frac{\Delta E}{\Delta x} \right\rangle = K\rho \frac{Z}{A} \frac{z^2}{\beta^2} \left[\ln\left(\frac{2m_e c^2 \beta^2}{I(1-\beta^2)} \right) - \beta^2 \right],$$

where z and β are the charge number and the velocity relative to the speed of light of the projectile ion, respectively. Z/A, ρ, and I are the charge-mass ratio, density and mean ionization potential of the target material, and K is a constant. Since the different ion types (primary ions and potential contaminants) would have the same specific energy, i.e. same velocity, downstream of the synchrotron, the relative energy deposition in the silicon layer of the different ions depends solely on the ratio of the squared charge number of the ions. Due to this z^2-dependence, well-differentiated energy depositions connected to different ion types are expected.

[2] R_{80} is characterized by the depth at the distal dose fall-off where the dose drops to 80% of the maximum dose level.

Post-processing of the data has to be carried out to identify and remove spurious signals that are neither caused by incident primary particles nor by contamination ions in the beam (e.g. signals caused by recoil nuclei in silicon or by overlapping/integrated signals of two or more ion tracks). This is necessary to allow for an unbiased quantitative analysis of beam purity. To facilitate this procedure, not only the energy deposition of single ions in one detector was measured, but track identification was performed by using a telescope consisting of three synchronized Timepix detectors. The set of detectors provides for each signal a spatial resolution better than the pixel pitch of 55 µm of the detector. The first detector was used to measure the energy deposition, while the last two detectors were used to measure the arrival time of the impinging particles. The time stamps on the last two detectors were used to identify coincident hits, and these coincidences were connected to the measured energy deposition by back-projection of the corresponding tracks onto the energy detector. In this way, signals due to recoils and other background which are not observed in all three detector layers, as well as overlapping signals from multiple tracks, can be identified and removed. The next step in the analysis is the generation of two-dimensional (2D) histograms of energy deposition in detector 1 on the first axis and the corresponding cluster size (defined as number of adjacent hit pixels) on the second axis. Since the cluster size is an additional parameter that helps to classify different signals, the final differentiation between signals caused by primary helium ions and signals caused by other ion types due to beam impurities is based on the 2D histogram and not only on the energy deposition information.

3 Results

3.1 Reference dosimetry

The dose response in the reference dosimetry measurements was evaluated with respect to the influence of the chamber type, readout device, ion type and set-up geometry. The intrinsic response variability of the ion chambers were not estimated. However, they are expected to be smaller than the uncertainty associated to the chamber correction factors and calibration. For example, the uncertainty budget for the computation of beam quality correction factors k_Q for carbon-ion beams has been estimated as 2.4% [21].

The response of the monitor chamber (employed to cut-off the irradiation) was used to evaluate the dosimetric reproducibility of the beam control system. The measured dose shows an average deviation of +0.02% and -0.02% from the requested dose for protons and carbon ions, respectively, with a relative variation of 0.09% and 0.03% (1 standard deviation). The ionization chamber-specific response averaged over different irradiations is presented in Figure 4 for the irradiation with proton and carbon-ion beams using different combinations of the readout devices. In the following, except when explicitly stated otherwise, the results obtained using the RW3 slab phantom are excluded from the analysis to avoid introducing a bias in the response with the Farmer chambers.

Figure 5 shows the influence of the chamber type. The dose response of the chamber EGG600 was, on average, 2.5% higher than the requested dose. The dose response of the chambers EGG908, F3641 and F1583 were lower than the requested dose by 3.2%,

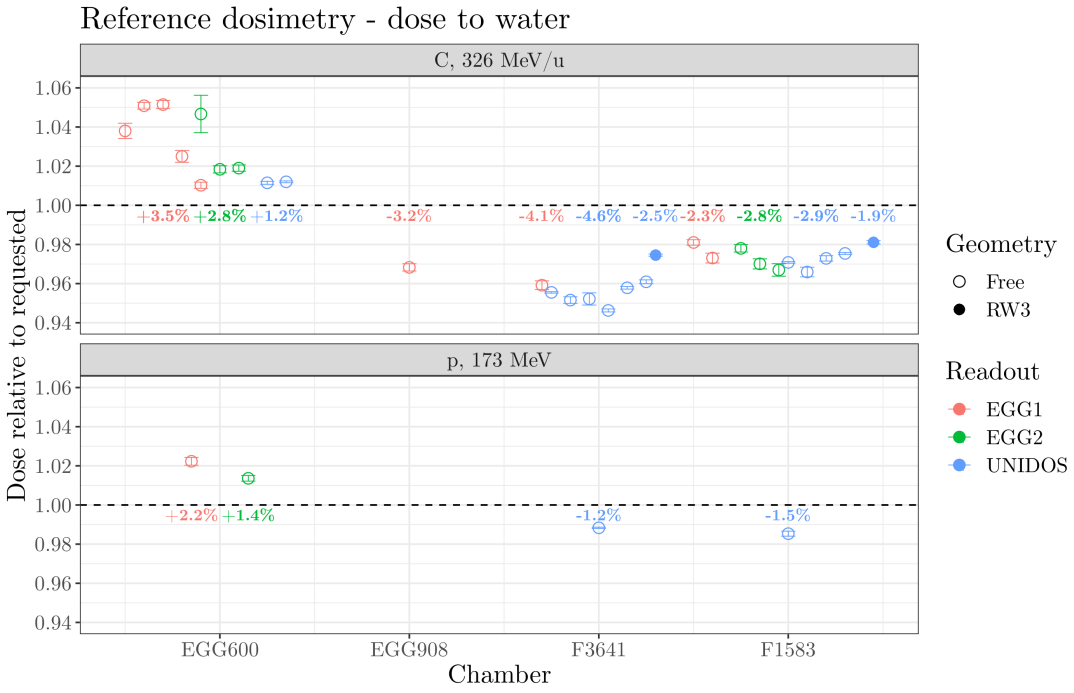

Figure 4. Mean dose response data over different runs for the "EGG" ionization chambers S/N 600 (EGG600) and S/N 908 (EGG908) and Farmer chambers S/N TM30013-03641 (F3641) and S/N TM30013-001583 (F1583). Colours are used to differentiate the readout device. Filled circles represent the measurements with the Farmer chamber placed inside the RW3 slab phantom.

3.7% and 2.5%, respectively. Approximately 5–6% difference between chamber EGG600 and the other chambers was observed. Tukey multiple pairwise-comparisons was used to evaluate the significance of the differences. Except for the pair comparison between EGG908 and each of the Farmer chambers, all other differences among the chambers are mutually significant.

Figure 6 shows the influence of the readout device on the response of the ionization chambers. The dose response obtained with the readout EGG1 is, on average, 1.3% higher than the requested dose. In contrast, the other two readouts show average dose response lower than the requested dose, -0.5% for EGG2, and -2.5% for UNIDOS. Mutually significant differences in the response depending on the readout device were observed. The response with UNIDOS is on average approximately 4% lower than the response using EGG1. Differences between EGG1 and EGG2 are smaller (1.8%).

The influence of the readout device segmented per chamber type is shown in Figure 7. The results show that the main effect observed for the depedence of the chamber response on the readout device is driven by the response of the chamber EGG600. In contrast, the response of the Farmer ionization chambers is substantially less sensitive to the specific readout device used.

Figure 8 shows the influence of the beam on the chamber response for 4 specific combinations of chamber and readout. Significant differences between the response to proton

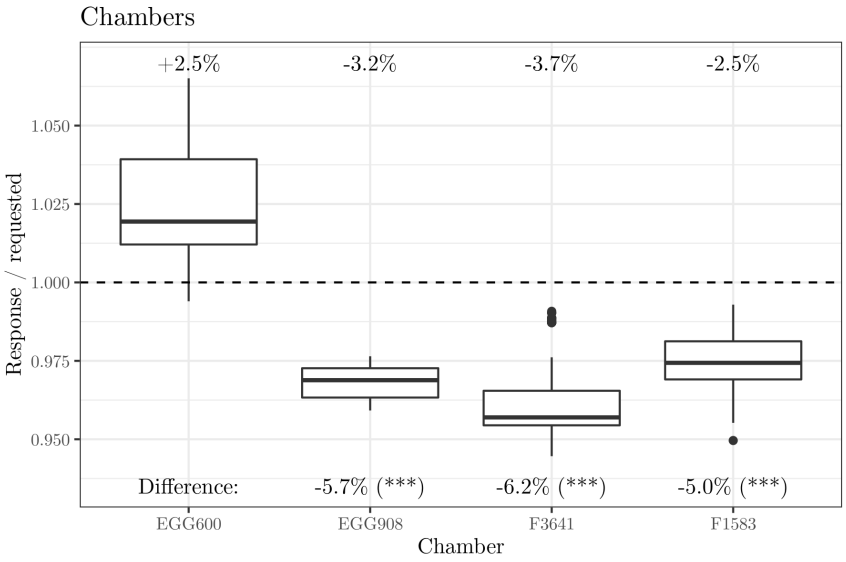

Figure 5. Influence of chamber type on the chamber dose response. Values on the top indicate the deviation w.r.t. the requested dose, while values on the bottom evaluate the significance of the difference in the results w.r.t. the results obtained with the reference chamber EGG600.

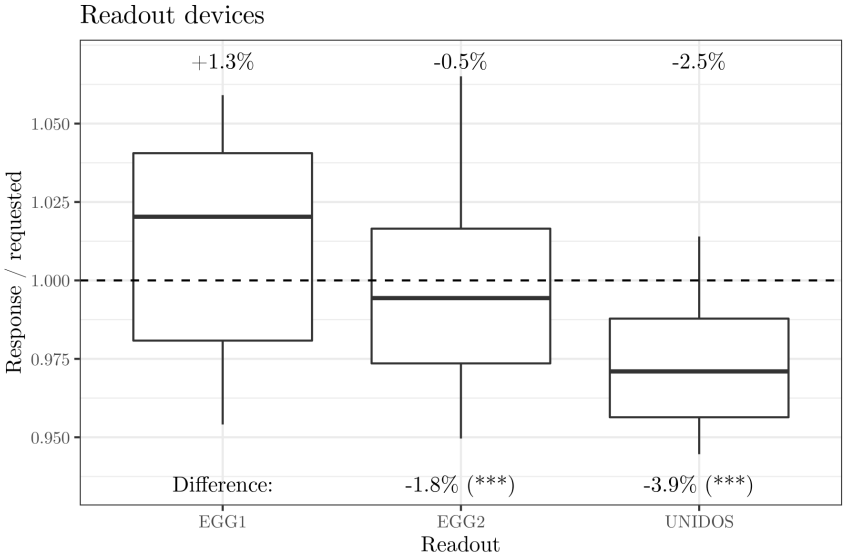

Figure 6. Influence of readout device on the chamber dose response. Values on the top indicate the deviation w.r.t. the requested dose, while values on the bottom evaluate the significance of the difference in the results w.r.t. the results obtained with the reference readout EGG1.

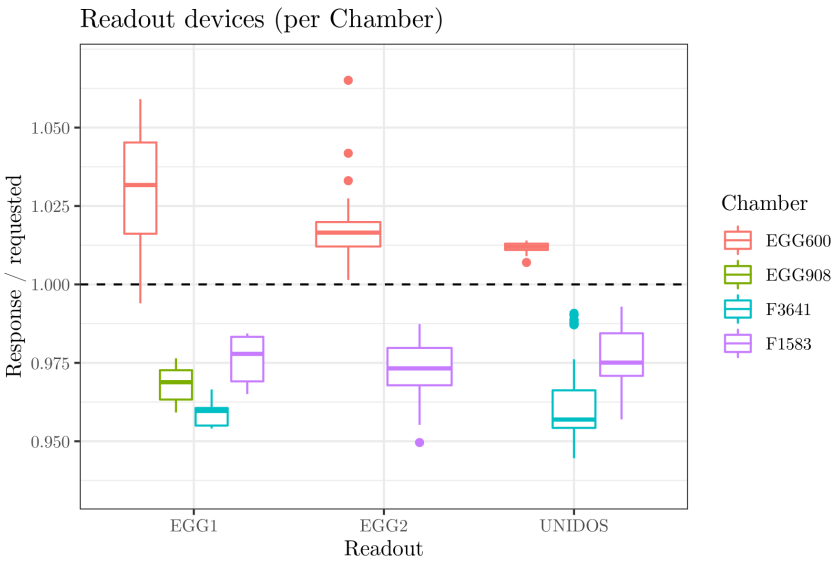

Figure 7. Influence of readout device on the chamber dose response segmented per chamber type.

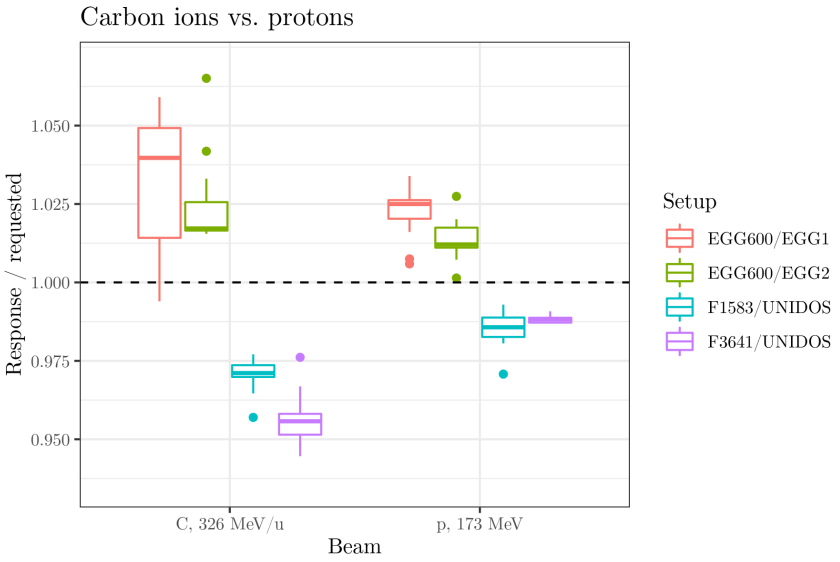

Figure 8. Influence of ion beam on the chamber response for 4 combinations of chamber and readout device.

and carbon-ion beams are observed. The response to protons is smaller for the EGG600 chamber with respect to the response to carbon ions, while the opposite effect is observed for the Farmer ionization chambers.

Figure 9 shows the influence of the geometry set-up on the response of the Farmer ionization chambers, i.e., free in air, or mounted inside the RW3 slab phantom. As expected, the variability of the chamber response is substantially reduced when the chamber is placed inside the RW3 slab phantom, followed by an increase of the response which is in line with

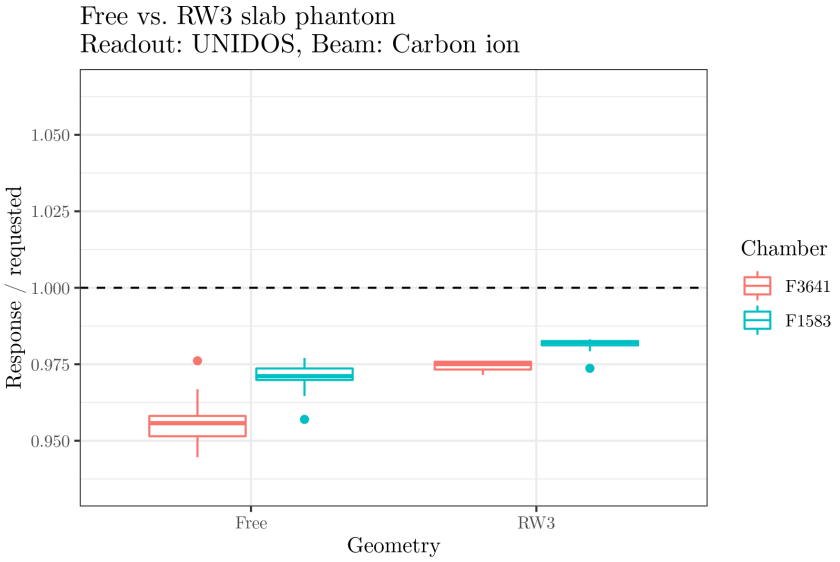

Figure 9. Influence of geometry on the dose response of the Farmer chambers using the UNIDOS readout for irradiation with carbon-ion beam.

the increase of stopping power due to the increase of material in the beam path.

The variability of the chamber response were evaluated with respect to chamber type and readout used. In each case, the variabilty was first corrected for the observed linear trend of the response as a function of time of irradiation for a given run. No significant differences in variability were observed due to the chamber type (see Figure 10). Regarding the impact of the readout device, UNIDOS shows significantly (3 fold) less variability across all chambers in comparison to the readout devices EGG1 and EGG2 (see Figure 11).

3.2 Lateral-dose profiles

Field homogeneity was evaluated by means of lateral-dose profile measurements in a 10×10 cm^2 central region. Figure 12 shows the lateral-dose profiles for 173 MeV proton and 326 MeV/n carbon-ion beams in the horizontal and vertical direction normalized to the response at the center of the field. The variation (1 standard deviation) of the chamber response for protons is 1.9% and 4.4% in the horizontal and vertical direction, respectively. For carbon ions, the variation is significantly lower corresponding to 1.1% and 0.8% in the horizontal and vertical directions, respectively. Despite the large uncertainty in the chamber response, a significant ($p < 0.05$) underlying dependence of the chamber response on the position in the field was observed for all cases. In particular, a large increase of dose towards the edge of the field (up to 15% higher at 50 mm distance from the center of the field) was observed for the proton beam in the vertical direction.

3.3 Depth-dose profiles and range in water

Figure 13 shows the measured depth-dose profiles for the 173 MeV proton beam. It should be emphasized that the beam settings at NSRL are manually adjusted in contrast to pre-defined

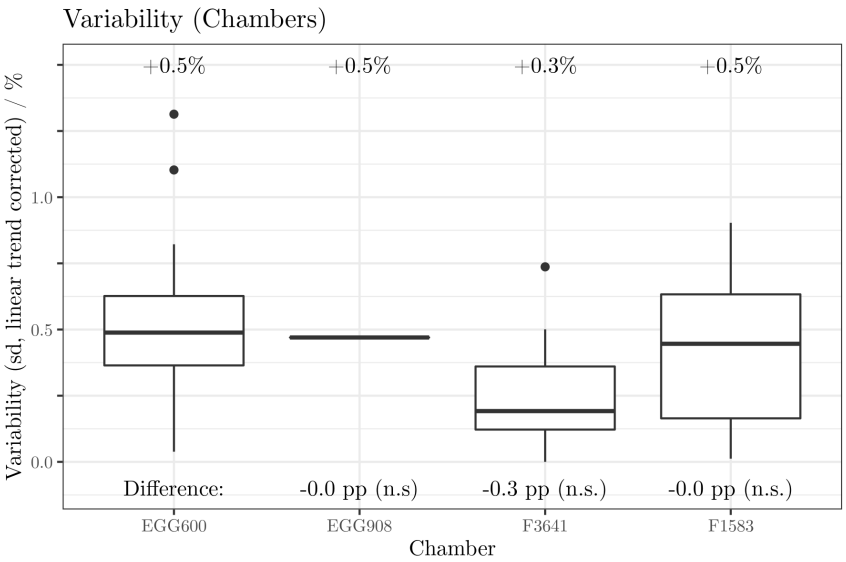

Figure 10. Influence of chamber type on response variability. The reponse variability is corrected by the linear trend of the response as a function of time of irradiation.

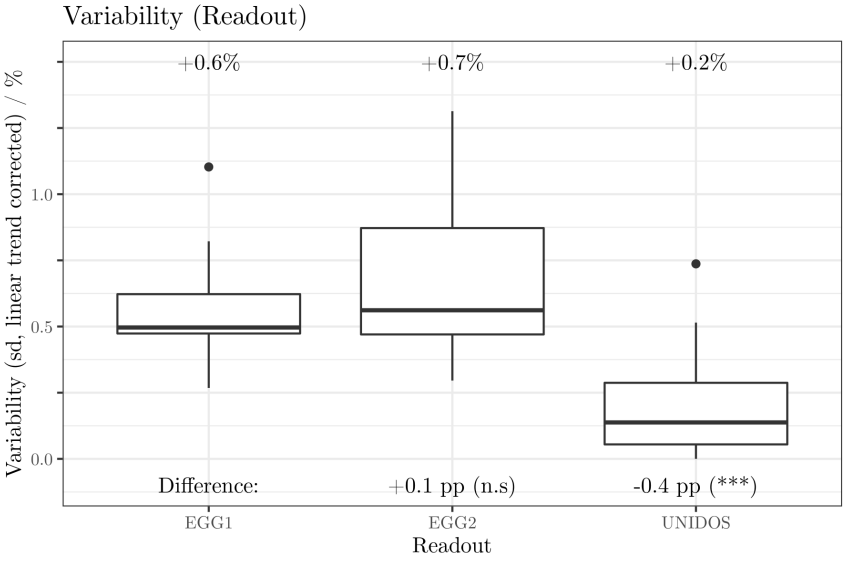

Figure 11. Influence of readout type on response variability. The reponse variability is corrected by the linear trend of the response as a function of time of irradiation.

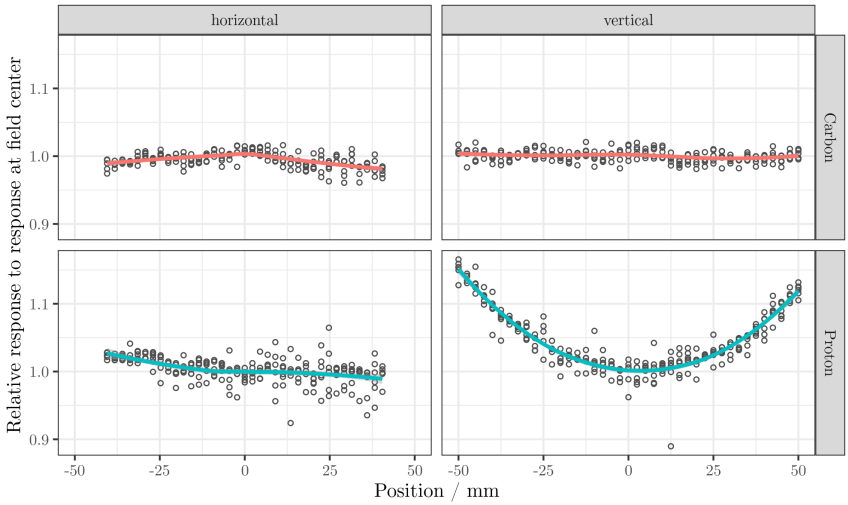

Figure 12. Chamber response relative to the response at the center of the field for 173 MeV proton and 326 MeV/n carbon-ion beams measured in horizontal and vertical direction.

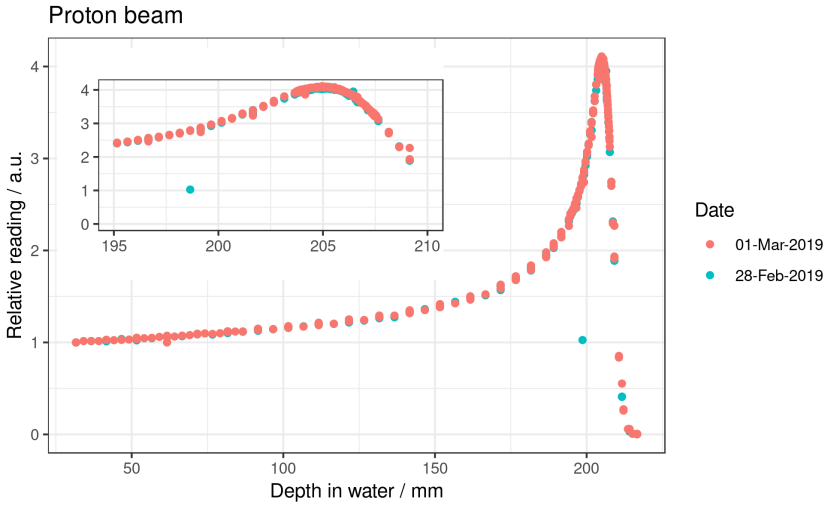

Figure 13. Depth-dose profile in water for the 173 MeV proton beam.

settings used in clinical facilities. Therefore, it is relevant to evaluate the reproducibility of the measurements. The results could be well reproduced in the two consecutive days with range in water of R_{80} = 207.2±0.5 mm in water (i.e., only 0.2% variation of range). The relative readings were obtained by averaging the chamber readings over three spills taken in sequence. During the measurements on February 28th, 2019 for the depth of 198.65 mm for the proton beam, the beam spill dropped over a period of two spills affecting the average relative reading as observed in Figure 13.

Figure 14 shows the measured depth-dose profiles for the 173 MeV/n helium-ion beam. Differently from the proton beam, the helium-ion beam was not stable compromising the measurements. The Bragg curve could only be measured in one day of the exper-

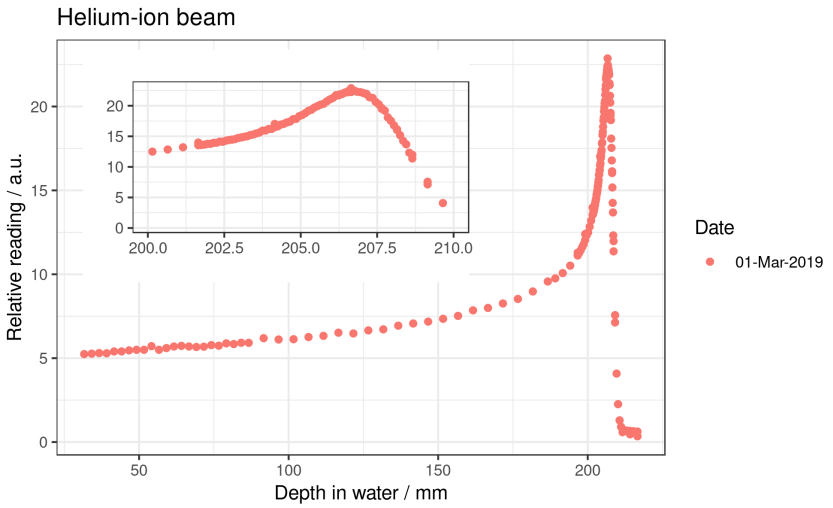

Figure 14. Depth-dose profile in water for 173 MeV/n helium-ion beam.

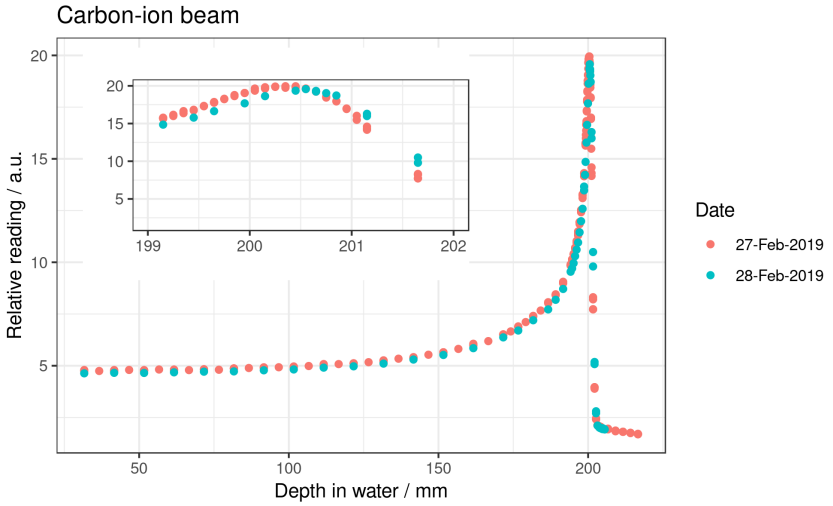

Figure 15. Depth-dose profile in water for 326 MeV/n carbon ion beam.

imental campaign. The 173 MeV/n helium-ion beam was observed to have a range of R_{80} = 207.4±0.6 mm in water.

Figure 15 shows the measured depth-dose profiles for 326 MeV/n carbon-ion beam. The range in water was observed to be R_{80} = 201.2±0.2 mm indicating a variation of R_{80} of only 0.1% in different days.

Figure 16 shows the depth-dose profile obtained by modulation of 217 MeV/n and 326 MeV/n carbon-ion beams using an in-house-machined modulator wheel. A relatively flat 25 mm-wide spread-out Bragg peak is achieved with the modulation indicating the capability of producing SOBP beams necessary for radiobiological experiments.

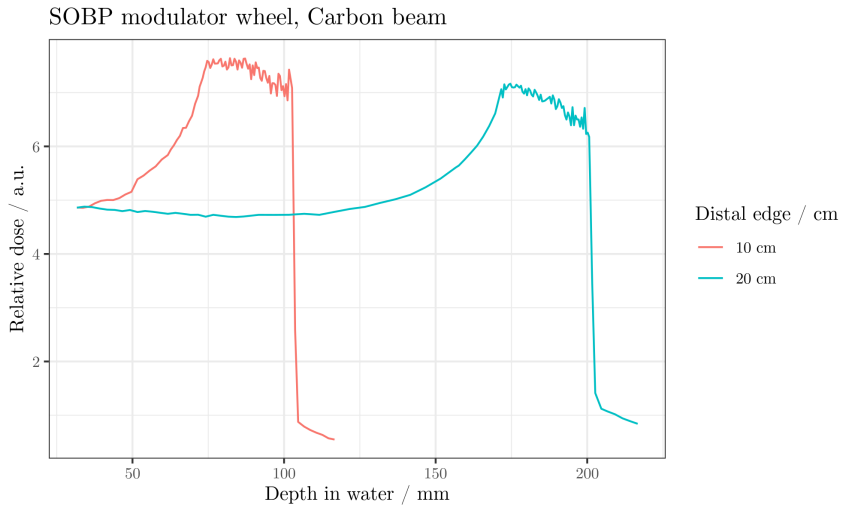

Figure 16. Depth-dose profile in water for 217 MeV/n and 326 MeV/n carbon-ion beam with an in-house-machined modulator wheel.

Table 2. Nominal thickness of binary range shifter layers, range in water (R_{80}), and WET.

Thickness (mm)	R_{80} (mm)	WET (mm)
0.25	201.05	0.1
0.5	200.85	0.3
1	200.35	0.8
2	199.25	1.9
4	197.15	4.0
8	192.95	8.2
16	184.75	16.4
32	168.35	32.8
64	135.25	65.9
128	70.55	130.6

3.4 WET of HDPE layers

The estimated WET of the individual HDPE layers of the binary range shifter is shown in Table 2 along with their nominal thickness. Unexpected small WET was observed for the thin layers indicating a WEPL of HDPE smaller than unity. Since the uncertainty in the WET as well as in the machined thickness of the HDPE layers are larger for the thin layers, only layers with nominal thickness $t \geq 8$ mm were selected to evaluate the WEPL of HDPE. This approach resulted in a mean value of 1.025 for the WEPL of the HDPE used in the range shifter.

Figure 17 shows the depth-dose profile measured in water with the Markus ionization chamber and the water-equivalent Bragg profiles obtained for carbon-ion beam using the binary range shifter and the two large planar ion chambers QC1 and QC3.

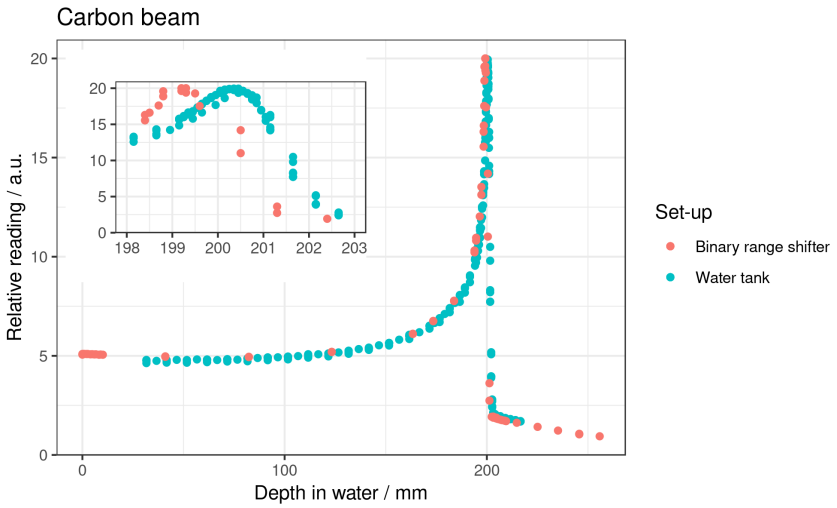

Figure 17. Depth-dose profile in water for 326 MeV/n carbon-ion beam and corrected Bragg curve obtained with the binary range shifter.

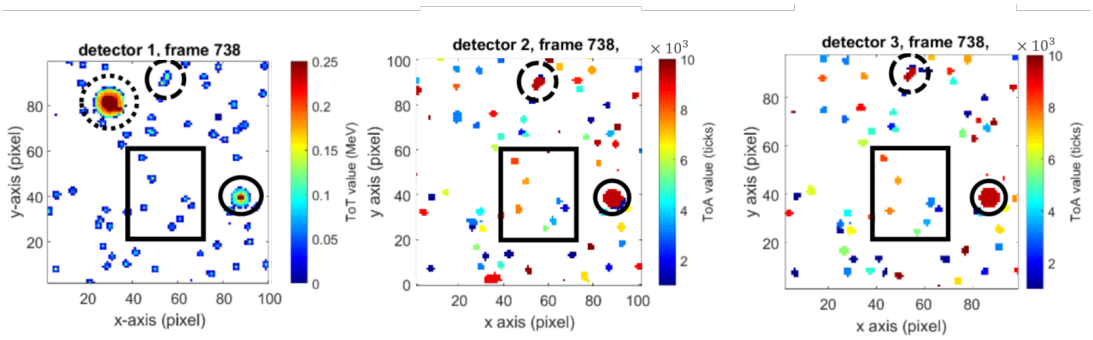

Figure 18. Example of raw data signals measured in detector 1, 2, and 3 within a time window of 1 ms. Squares indicate matched signals caused by primary helium ions; full circles indicate three matched signals that are assigned to an impurity ion; the dotted circle indicates a signal on detector 1 that is most likely caused by a recoil nucleus; and the dashed circles indicate overlapping signals of two ions. Signals marked by dotted and dashed circles are rejected from further analysis.

3.5 Purity of the helium-ion beam

The results of the purity analysis of a 173 MeV/n helium-ion beam is presented below. Figure 18 shows one data set of a 1 ms-long acquisition, where signals of primary helium ions (full square), a signal of a heavier ion due to impurities (full circle), and two types of rejected signals (dashed/dotted circles) are marked. The assignment of the signals to heavier ions is based on the much higher energy deposition in detector 1 compared to the energy deposition of the primary helium ions in that detector. The dotted circle indicates a signal that is only measured in detector 1 and is most probably a recoil nucleus, being rejected from the further analysis. The dashed circles indicate overlapping signals of two ions. The summed energy deposition of the two ions could be mistakenly registered as the energy deposition of an impurity ion, and therefore these signals are also rejected.

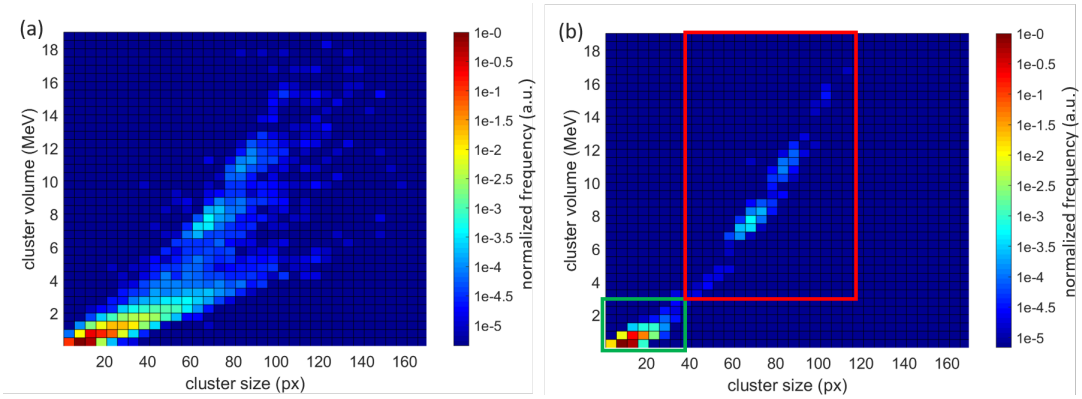

Figure 19. Two-dimensional histograms of measured signals, in which they are sorted by their size and their energy deposition. Panel (a): signals measured by detector 1 before the identification and rejection of unwanted background (e.g. recoil nuclei or overlapping signals). Panel (b): signals measured by detector 1 after identification and rejection of unwanted background. The signals in the red square can be related to beam impurities with significantly higher energy depositions than the primary helium ions marked by the green square.

Figure 19 shows the comparison of the 2D histograms of measured signals sorted by their energy deposition and their cluster size obtained (a) prior and (b) after applying the rejection of unwanted background. The background visible in Figure 19(a) would bias the determination of the amount of impurities if not suppressed underlining the importance of background-suppression. In Figure 19(b) a clear distinction between primary helium ions and contamination ions is visible as indicated by the green and red squares. The red square includes signals with energy depositions and cluster sizes above 3 MeV and 40 px, respectively. These energy depositions above 3 MeV by the contamination ions are significantly higher than the energy depositions by the primary helium ions (99.996% of helium ions have energy depositions below 2 MeV).

Figure 20 presents a three dimensional visualization of the background-suppressed signals shown in Figure 19(b). It facilitates the visual identification of the different contributions from primary helium ions and beam impurities.

The evaluation of the amount of impurity ions (inside the red square in Figures 19(b) and 20(a)) with respect to the amount of helium ions (inside the green square) yields

$$\frac{\text{Impurities}}{\text{Helium ions}} = \frac{(0.503 \pm 0.022\,_{\text{stat}} \pm 0.005\,_{\text{sys}}) \times 10^3}{(272.91 \pm 0.52\,_{\text{stat}} \pm 0.38\,_{\text{sys}}) \times 10^3}$$

corresponding to a contamination level of $0.184 \pm 0.008\,_{\text{stat}} \pm 0.002\,_{\text{sys}}\%$ where the uncertainty is divided into statistical and systematic contributions. The statistical uncertainty comprises the count statistics based on the Poisson distribution. The systematic uncertainty is calculated by varying the vertices of the rectangles in the 2D histogram that are used to quantify the amount of primary helium ions and impurity ions (cf. Figures 19 and 20).

To identify the ion types of the contaminants, the mean energy deposition of the different contamination peaks $< \Delta E_{\text{cont}} >$ (cf. Figure 20 (a)) can be compared with the

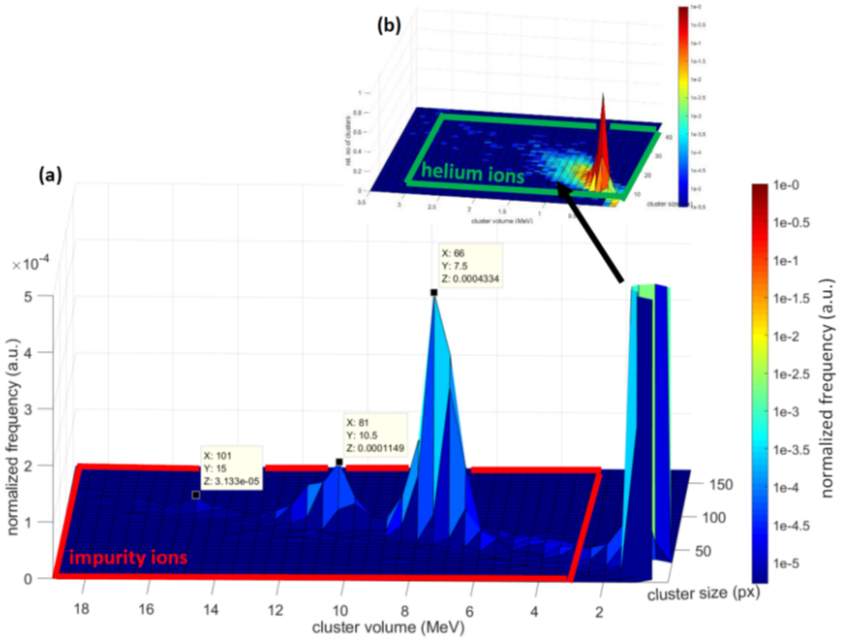

Figure 20. Distribution of the relative number of clusters as a function of cluster volume and cluster size. To make the peak heights of the beam impurities visible (about three orders of magnitude lower then the peak for primary helium ions), the scale of the relative number of clusters (vertical axis) in panel (a) was set to 5×10^{-4}. At this scale, the peak of the helium ions is drastically clipped. The inset (b) shows the unclipped distribution of helium clusters.

mean energy deposition of the primary helium ions $< \Delta E_{\mathrm{He}} >$. Taking the ratio of the Bethe-Bloch equation (see Section 2.6) for the contaminant and for helium ions, the atomic number of the contaminants z_{cont} can be derived as

$$z_{\mathrm{cont}} = \sqrt{z_{\mathrm{He}}^2 \frac{\langle \Delta E_{\mathrm{cont}} \rangle}{\langle \Delta E_{\mathrm{He}} \rangle}}.$$

The mean energy depositions in the measurements were $\langle \Delta E_{\mathrm{He}} \rangle = (0.41 \pm 0.03)\,\mathrm{MeV}$, $\langle \Delta E_{\mathrm{cont,I}} \rangle = (7.63 \pm 0.53)$ and $\langle \Delta E_{\mathrm{cont,II}} \rangle = (11.02 \pm 0.77)$ for helium ions, and the two most abundant contaminants. The uncertainties were estimated based on a previous study on energy deposition of ions with therapeutic initial energies for the exact same detector [22]. Accounting for the mean energy depositions of the ions, the derived equation for the atomic number of a contaminant and error propagation, we obtained within 95% confidence intervals the atomic numbers of the contaminants as 8.6±0.9 and 10.4±1.0. These contaminants are most likely oxygen and neon ions, respectively, as these ions can be delivered at the same rigidity as the helium ions. Besides, neon is known to be a likely contaminant as it is hard to remove all the neon from the helium supply gas.

4 Conclusions

Measurements of reference dosimetry comparing ionization chambers and electrometers from NSRL and calibrated complementary devices were performed for proton and carbon-ion beams. The dose response of the monitor chamber used to cut-off the irradiation indicates a highly stable beam. The dose response of the chamber EGG600 was, on average, 2.5% higher than the requested dose. Relative deviations of the order of 6% on the measured dose was observed across chambers, while the choice of readout device may result in relative differences of measured dose up to 4%. Significant differences between the response to proton and carbon-ion beams are observed depending on the particular ionization chamber. Lateral-dose profile measurements in air in the central $10 \times 10\,\mathrm{cm}^2$ region showed large dependence of the chamber response on the position in the field for the irradiation with protons. Conversely, for the irradiation with carbon ions, the irradiation field is more homogeneous with small dose variations. However, more data are needed to quantity this variation and obtain an uncertainty estimate. Regarding depth-dose measurements, results indicate high reproducibility with R_{80} varying by only 0.2% for proton beams and 0.1% for carbon-ion beams. The WET values of the layers of the binary range shifter were estimated and a mean WEPL of 1.025 for HDPE was obtained. Contamination of the helium beam was evaluated and the presence of ions heavier than helium is less than 0.2%.

Acknowledgments

We would like to thank NIH for the financial support. The support from PTW/PTW US, in special, Axel Hoffmann, with the logistic of the equipment from DKFZ is highly appreciated. The work at NSRL is supported by NASA (Contract No. T570X) and performed under the United State Department of Energy Contract No. DE-AC02-98CH10886.

References

[1] J. Miller and C. Zeitlin, *Twenty years of space radiation physics at the BNL AGS and NASA Space Radiation Laboratory*, *Life Sciences in Space Research* **9** (2016) 12–18.

[2] C. L. Tessa, M. Sivertz, I.-H. Chiang, D. Lowenstein and A. Rusek, *Overview of the NASA space radiation laboratory*, *Life Sciences in Space Research* **11** (2016) 18–23.

[3] K. D. Held, E. A. Blakely, M. D. Story and D. I. Lowenstein, *Use of the NASA Space Radiation Laboratory at Brookhaven National Laboratory to Conduct Charged Particle Radiobiology Studies Relevant to Ion Therapy*, *Radiation Research* **185** (2016) 563–567.

[4] M. Durante, H. Paganetti, A. Pompos, S. F. Kry, X. Wu and D. R. Grosshans, *Report of a National Cancer Institute special panel: Characterization of the physical parameters of particle beams for biological research*, *Medical Physics* **46** (2019) e37–e52.

[5] E. Draeger, A. Sawant, C. Johnstone, B. Koger, S. Becker, Z. Vujaskovic et al., *A dose of reality: How 20 years of incomplete physics and dosimetry reporting in radiobiology studies may have contributed to the reproducibility crisis*, *International Journal of Radiation Oncology, Biology, Physics* **106** (Feb, 2020) 243–252.

[6] X. Llopart, R. Ballabriga, M. Campbell, L. Tlustos and W. Wong, *Timepix, a 65k programmable pixel readout chip for arrival time, energy and/or photon counting measurements*, *Nucl. Instrum. Meth. A* **581** (2007) 485–494.

[7] R. Ballabriga, M. Campbell and X. Llopart, *Asic developments for radiation imaging applications: The medipix and timepix family*, *Nucl. Instrum. Meth. A* **878** (2018) 10–23.

[8] N. Stoffle, L. Pinsky, M. Kroupa, S. Hoang, J. Idarraga, C. Amberboy et al., *Timepix-based radiation environment monitor measurements aboard the international space station*, *Nuclear Instruments and Methods in Physics Research Section A: Accelerators, Spectrometers, Detectors and Associated Equipment* **782** (2015) 143 – 148.

[9] M. Kroupa, A. Bahadori, T. Campbell-Ricketts, A. Empl, S. M. Hoang, J. Idarraga-Munoz et al., *A semiconductor radiation imaging pixel detector for space radiation dosimetry*, *Life Sciences in Space Research* **6** (2015) 69 – 78.

[10] C. Granja, S. Polansky, Z. Vykydal, S. Pospisil, A. Owens, Z. Kozacek et al., *The satram timepix spacecraft payload in open space on board the proba-v satellite for wide range radiation monitoring in leo orbit*, *Planetary and Space Science* **125** (2016) 114 – 129.

[11] K. Gwosch, B. Hartmann, J. Jakubek, C. Granja, P. Soukup, O. Jäkel et al., *Non-invasive monitoring of therapeutic carbon ion beams in a homogeneous phantom by tracking of secondary ions*, *Physics in Medicine and Biology* **58** (may, 2013) 3755–3773.

[12] R. Félix-Bautista, T. Gehrke, L. Ghesquière-Diérickx, M. Reimold, C. Amato, D. Turecek et al., *Experimental verification of a non-invasive method to monitor the lateral pencil beam position in an anthropomorphic phantom for carbon-ion radiotherapy*, *Physics in Medicine & Biology* **64** (sep, 2019) 175019.

[13] G. Aricò, T. Gehrke, R. Gallas, A. Mairani, O. Jäkel and M. Martišíková, *Investigation of single carbon ion fragmentation in water and PMMA for hadron therapy*, *Physics in Medicine & Biology* **64** (mar, 2019) 055018.

[14] T. Gehrke, R. Gallas, O. Jäkel and M. Martišíková, *Proof of principle of helium-beam radiography using silicon pixel detectors for energy deposition measurement, identification, and tracking of single ions*, *Medical Physics* **45** (2018) 817–829, [https://aapm.onlinelibrary.wiley.com/doi/pdf/10.1002/mp.12723].

[15] A. C. Kraan, *Range verification methods in particle therapy: Underlying physics and monte carlo modeling*, *Frontiers in Oncology* **5** (2015) 150.

[16] F. Horst, G. Aricò, K.-T. Brinkmann, S. Brons, A. Ferrari, T. Haberer et al., *Measurement of* ^{4}He *charge- and mass-changing cross sections on h, c, o, and si targets in the energy range 70–220 mev/u for radiation transport calculations in ion-beam therapy*, *Phys. Rev. C* **99** (Jan, 2019) 014603.

[17] G. Aricò, T. Gehrke, J. Jakubek, R. Gallas, S. Berke, O. Jäkel et al., *Investigation of mixed ion fields in the forward direction for 220.5 MeV/u helium ion beams: comparison between water and PMMA targets*, *Physics in Medicine & Biology* **62** (oct, 2017) 8003–8024.

[18] M. Rovituso, C. Schuy, U. Weber, S. Brons, M. A. Cortés-Giraldo, C. L. Tessa et al., *Fragmentation of 120 and 200 MeV u-14he ions in water and PMMA targets*, *Physics in Medicine and Biology* **62** (jan, 2017) 1310–1326.

[19] H. Bethe, *Zur theorie des durchgangs schneller korpuskularstrahlen durch materie*, *Annalen*

der Physik **397** (1930) 325–400,
[https://onlinelibrary.wiley.com/doi/pdf/10.1002/andp.19303970303].

[20] Particle Data Group collaboration, M. Tanabashi, K. Hagiwara, K. Hikasa, K. Nakamura, Y. Sumino, F. Takahashi et al., *Review of particle physics*, *Phys. Rev. D* **98** (Aug, 2018) 030001.

[21] L. N. Burigo and S. Greilich, *Impact of new ICRU 90 key data on stopping-power ratios and beam quality correction factors for carbon ion beams*, *Physics in Medicine & Biology* **64** (sep, 2019) 195005.

[22] T. Gehrke, L. Burigo, G. Arico, S. Berke, J. Jakubek, D. Turecek et al., *Energy deposition measurements of single1h,4he and12c ions of therapeutic energies in a silicon pixel detector*, *Journal of Instrumentation* **12** (apr, 2017) P04025–P04025.